Physicochem. Probl. Miner. Process., 62(1), 2026, 216813

http://www.journalssystem.com/ppmp

Physicochemical Problems of Mineral Processing

ISSN 1643-1049

Influence of oxidation regulation on flotation desulfurization of fine coking coal

Hui Hou [1], Wei Cheng [2,3,4], Manqing Ai [2,3,4]

[1] College of Resources and Environmental Engineering, Guizhou University, Guiyang, 550025, China

[2] Mining College, Guizhou University, Guiyang 550025, China

[3] National & Local Joint Laboratory of Engineering for Effective Utilization of Regional Mineral Resources from Karst Areas, Guiyang 550025, China

[4] Guizhou Key Lab of Comprehensive Utilization of Nonmetallic Mineral Resources, Guiyang 550025, China

Corresponding author: wcheng1@gzu.edu.cn (Wei Cheng)

Abstract: Desulfurizing high-sulfur coking coal, a strategically valuable resource, optimizes its utilization and reduces environmental sulfur emissions. This study investigated moderate oxidation to enhance flotation desulfurization of a fine coking coal (1.66% sulfur) from Guizhou, China. Without oxidant, single flotation of -0.2 mm feed yielded clean coal (89.91% yield, 1.32% sulfur and 11.89% ash), while adding 500 g/t oxidizing agent with 9-minute conditioning improved desulfurization performance (90.64% yield, 1.10% sulfur, 11.21% ash). Adopting a single roughing-single cleaning circuit further reduced the sulfur content of the final clean coal (84.73% yield, 1.04% sulfur, 11.37% ash). Flotation tests of pure minerals, combined with coating angle, induction time, microcalorimetry, AFM and Raman revealed oxidation significantly modifies pyrite. The contact angle decreased (75.6° to 31.3°), coating angle decreased (103.70° to 57.85°), induction time increased (5 ms to 50 ms), and wetting heat increased (1.85 J/g to 3.66 J/g). This is attributed to hydrophilic compound formation (e.g., $Fe2(SO_4)_3$, $CaSO_4$, $Fe(OH)_3$) on pyrite. Deposited hydrophilic species enhance pyrite hydrophilicity, leading to reduced floatability. The oxidation of the slurry significantly governs the amount of hydrophilic species formed on pyrite. Moderate oxidation effectively regulates their formation, enhancing pyrite depression. This provides a scientific basis for deep desulfurization technologies.

***Keywords*:** coking coal, flotation, desulfurization, oxidation regulation

1. Introduction

Sulfur is widely recognized as one of the major hazardous contaminant elements in coal, playing a significant role in affecting coal quality and posing potential risks during coal utilization processes (Chou, 2012; Zhang et al., 2014). The direct combustion or conversion processes of high-sulfur coal release substantial amounts of sulfur oxides, causing atmospheric pollution and equipment corrosion, which pose significant threats to industrial and agricultural production as well as human health (Munawer, 2018; Dai et al., 2021; Debiagi et al., 2021; Prakash et al., 2023). Coal desulfurization enhances calorific value, reduces subsequent pollution control costs, and mitigates environmental risks (Tang et al., 2020). Furthermore, many downstream users impose strict sulfur limits; for example, coking coal typically requires S≤1.0% (Mu et al., 2020). Thus, developing efficient coal desulfurization technologies is crucial for improving resource utilization efficiency and reducing environmental impact, thereby aligning with sustainable development goals (Xia et al., 2017).

Guizhou Province boasts the richest coal resources in southern China, with large reserves and diverse coal types (Hou et al., 2024). In 2024, Guizhou's verified coal reserves stood at 80.617 billion tons, ranking fifth nationally. This includes 13.960 billion tons of coking coal reserves, placing third nationwide (Hou et al., 2025). However, Guizhou coal generally exhibits high sulfur content, with high-sulfur coal (totalt sulfur >3%) accounting for 35% of reserves (Jiao et al., 2023). This poses a major

DOI: 10.37190/ppmp/216813

challenge to clean and efficient utilization of coal resources. Notably, a portion of this high-sulfur coal comprises coking coal (e.g., coking coal in Liuzhi and Shuicheng areas contains sulfur 2-6%) (Chou 2012). Failure to reduce its sulfur content below 1% would force these valuable coking coal resources to be used as thermal coal, resulting in resource waste and economic losses.

Sulfur in coal primarily occurs as pyritic sulfur (KAawatra et al., 1992; Diehl et al., 2012), making pyrite removal the primary aim of coal desulfurization (Qi et al., 2020). Conventional gravity separation methods (e.g., dense medium separation, jigging) struggle to achieve sufficiently low sulfur levels in clean coal when processing coarse coal (Phengsaart et al., 2023). Conversely, flotation effectively separates fine and ultrafine coal by exploiting surface property differences between pyrite and coal particles (Heet al., 2018; Ercan 2018). However, previous studies indicate that pyrite in coal (coal-pyrite) exhibits surface properties similar to coal (Hou et al., 2025), making it more floatable than common pyrite (Li et al., 2022). In coal slime flotation systems, it readily reports to the froth alongside coal particles, significantly reducing desulfurization efficiency (Zhao et al., 2021; Qi et al., 2019). Thus, adding depressants to enhance the depression of coal-pyrite is a critical aspect of desulfurization during coal slime flotation.

Lime (active component CaO) is a common pyrite depressant in coal slime flotation. Extensive studies confirm that adding lime to the pulp significantly reduces sulfur content in clean coal (Cheng et al., 2024; Zhang et al., 2020). Liao et al. attributed lime's depression of pyrite to the adsorption of Ca^{2+} and $Ca(OH)^{+}$ onto its surface under alkaline conditions, enhancing hydrophilicity. Cyanides, $Na_2S_2O_3$, $CaCl_2$, and $ZnSO_4$ also exhibit depressive effects (Li et al. 2022; Guo et al., 2014). Organic depressants like starch, vitamin C, thioglycolic acid, carboxymethyl cellulose, pyrogallol, and sodium humate inhibit pyrite, with starch showing relatively good efficacy (Han et al., 2019; Zhou et al., 2019; Bulut et al., 2012; Brenton, Chimonyo et al., 2020; Wang et al., 2023). However, organic depressants are less practically applied due to higher costs. Additionally, adding oxidants (e.g., $KMnO_4$, H_2O_2, $Ca(ClO)_2$, $KHSO_5$, $Fe_4[Fe(CN)_6]_3$) promotes pyrite surface oxidation, achieving depression (Yang et al., 2022; Zhao et al., 2022; Cao, et al., 2024; Jiang et al., 2022; Bai et al., 2019). Current research explores combining depressants with oxidants to enhance pyrite depression. However, these studies primarily focus on pyrite depression in polymetallic sulfide flotation, with limited research on desulfurization via fine coal flotation (Gan et al., 2023; Chen et al., 2024).

A coal preparation plant in Guizhou Province processes high-sulfur fine coking coal via flotation. However, the sulfur content of the clean coal remains relatively high sulfur 1.66%, failing to meet coking coal quality standards. This study investigates this flotation clean coal, aiming to enhance the depression of coal-pyrite and improve desulfurization efficiency by implementing oxidation conditioning of the flotation pulp. Furthermore, multiple characterization techniques are employed to elucidate the alteration in surface wettability of coal-pyrite under oxidation, offering a scientific basis for deep desulfurization of similar high-sulfur coals via flotation.

2. Samples and testing methods

2.1. Samples

2.1.1. Coal sample

The feed for flotation tests was collected from the clean coal product of a coking coal preparation plant's flotation circuit. The sample was air-dried, thoroughly homogenized, riffled, sealed in bags, and stored for later use. Analysis showed the air-dried basis moisture 2.28%, dry basis ash 12.72%, and dry basis total sulfur 1.66%. Its dry ash-free basis volatile 19.92%, and caking index 66 classified it as coking coal. The result of the sizing analysis of the feed was shown in Table 1. The feed exhibited a predominantly fine particle size distribution, with low coarse particle content (+0.25 mm accounts for 8.68%) and high fines content (-0.075 mm accounts for 53.02%). Intermediate size fractions showed relatively higher ash and sulfur contents. No significant correlation existed between sulfur and ash. Inorganic sulfur (pyritic + sulfate sulfur), constituting approximately 92.78% of total sulfur, was the dominant form, while organic sulfur accounted for only 7.22% (Table 2). This sulfur distribution theoretically supports the feasibility of desulfurization by flotation.

Table 1. Screen analysis of the feed

Size fraction / mm	yield/%	sulfur/%	ash content/%
+0.25	8.68	1.13	11.71
-0.25+0.15	19.74	1.39	19.21
-0.15+0.075	18.56	1.71	15.57
-0.075+0.045	17.09	2.12	13.80
-0.045+0.038	2.70	2.06	12.83
-0.038	33.23	1.48	10.03
Sum.	100	1.60	13.73

Table 2. Content of sulfur forms and total sulfur in raw coal, %

S_t	S_s	S_P	S_o
1.66	0.02	1.52	0.12

2.1.2. Coal-pyrite

Coal-pyrite crystals with relatively coarse grains were hand-picked from the raw coal of the preparation plant to prepare pure mineral flotation samples. After grinding, impurities (primarily coal particles) were manually removed under a microscope. The purified pyrite was then ultrasonically cleaned in deionized water, rinsed with absolute ethanol, and dried at low temperature. For bulk coal-pyrite samples, one surface was ground and polished to create a smooth test surface. Powder samples were pulverized to -0.075 mm using a vibratory mill for subsequent use. As shown in Fig. 1, XRD analysis of the purified pyrite revealed diffraction patterns highly consistent with the FeS_2 reference standard (PDF#71-0053). XRF analysis indicated a combined S and Fe content of 97.55% (corresponding to a calculated pyrite content of 95.14%), with minor amounts of C, Si, Al, and trace K and Ca (Table 3). These results confirm the high purity of the sample.

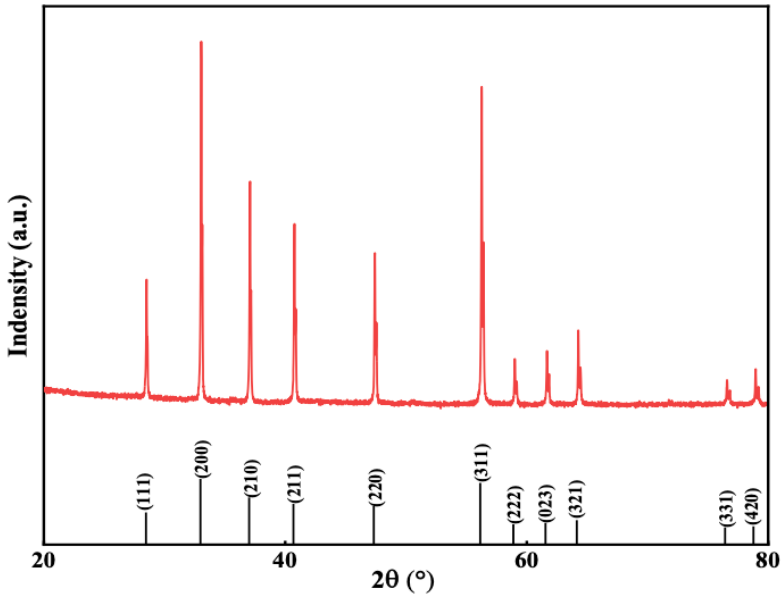

Fig. 1. Coal pyrite XRD diffractogram

Table 3. Chemical composition of the pyrite sample

Component	S	Fe	Al	Si	K	Ca
content/%	50.74	46.81	0.23	0.42	0.007	0.04

2.2. Testing methods

2.2.1. Pure mineral flotation

Pure mineral flotation tests were conducted using a laboratory-scale flotation machine (Model XFGCII, Jilin Exploration Machinery Factory, China) with a 45 mL flotation cell. A 2 g sample of pyrite powder, ground to a particle size of minus 0.075 mm, was weighed and introduced into the flotation cell. Subsequently, 40 mL of deionized water was added. After stirring for 60 s, an oxidizing agent was added to perform slurry oxidation treatment. Following this, reagents were sequentially added in the following order: a depressant (acting time: 120 s), a collector (acting time: 60 s), and a frother (acting time: 60 s). Air was then introduced, and froth was continuously scraped. The flotation products were filtered and subsequently placed in a vacuum drying oven at 45±1 ℃ until constant weight was achieved.

2.2.2. Coal slime flotation

Coal slime flotation tests were conducted in a single-cell flotation machine (Model RK/FD, Wuhan Rock Grinding Equipment Manufacturing Co., Ltd., China) with a flotation cell volume of 0.75 L. A a series of 3 exploratory tests were performed for the same feed, Measurements were carried out on the yield, ash content, and sulfur content of both clean coal and tailings, and we found that the experimental errors were constrained within the acceptable range. The pulp density was maintained at 45 g/L. Following the procedure established in the pure mineral flotation tests, reagents were added sequentially: an oxidizing agent (H_2O_2 or $Ca(ClO)_2$), a depressant (CaO, acting time: 180 s), a collector (kerosene, acting time: 60 s), and a frother (2-octanol, acting time: 60 s). Flotation was then performed for 180 s with air supply.

2.2.3. Mineral composition determination

The phase composition and crystallographic characteristics of the pyrite samples were analyzed using X-ray diffraction (XRD). The measurement parameters were set as follows: step size of 0.02°, scan rate of 2 °/min, scanning range of $10° \leq 2\theta \leq 80°$, tube voltage of 40 kV, and tube current of 40 mA. Whole-pattern fitting analysis was performed using Jade 6.5 software.

2.2.4. Contact angle measurement

The surface contact angle of the pyrite samples was measured using a contact angle goniometer (Model HARKE-SPCAX3, Harke Testing Instrument Factory, Beijing, China) employing the sessile drop method. Bulk pyrite samples were selected, ground, and polished. The polished surfaces were then immersed in collector solutions of varying concentrations for 10 minutes, corresponding to the flotation conditions. After air-drying at room temperature, the contact angle was measured. Three measurements were performed for each sample, and the arithmetic mean was calculated.

2.2.5. Coating angle and induction time

The coating angle measurement system is illustrated in Fig. 2, primarily comprising a high-speed CMOS camera, a microliter syringe system, a capillary tube (inner diameter: 2.00 ± 0.01 mm), a quartz reaction cell (3.5×3.5×5 cm), and a magnetic stirring system. The experimental procedure was as follows: First, 1 g of pyrite samples with varying degrees of oxidation (particle size <0.075 mm) was weighed and placed into the quartz cell. Subsequently, 40 mL of deionized water was added and stirred for 2 min at a speed of 500 r/min. Bubble images were recorded at the corresponding time, and the measured θ value represents the coating angle. For the induction time test, 1 g of pyrite powder treated with oxidizing agents at different concentrations was added to the test chamber, ensuring it was evenly distributed across the bottom. Deionized water was then introduced. A microliter syringe was employed to generate uniformly sized bubbles, which were gently lowered downward. The bubble was held in contact with the mineral particles for a specific duration and then retracted to its initial position. The attachment status of particles to the bubble surface was meticulously observed using an industrial camera. The contact duration between the bubble and the particle at the moment of attachment was

defined as the induction time (Li et al., 2018). Specific test details followed the methodology described in reference (Huang 2025).

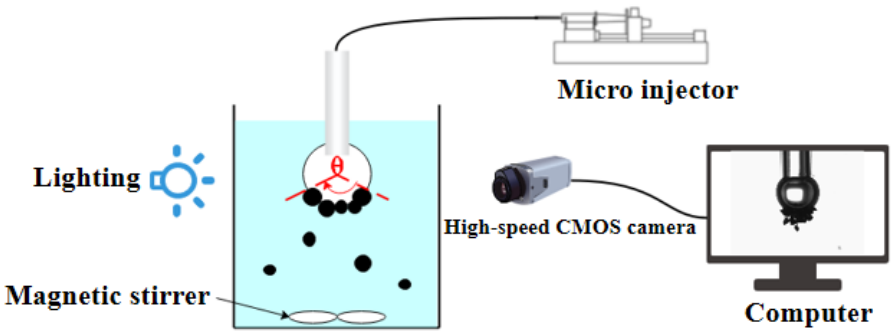

Fig. 2. Bubble-particle coating angle test diagram (Huang, 2025)

2.2.6. Microscopic confocal raman spectroscopy analysis

Polished bulk pyrite samples were first immersed in an oxidizing agent solution for 10 minutes. After immersion, the samples were separated from the solution by vacuum filtration and subsequently dried at low temperature. The treated samples were then immersed in a depressant solution for a further 1 minute. Following this second immersion, vacuum filtration and low-temperature drying were repeated. Finally, the processed samples were placed on glass slides and positioned under the objective lens for spectral acquisition.

2.2.7. Atomic force microscopy (AFM)

Pyrite was cut into block samples measuring 10×10×5 mm and subjected to fine surface polishing. The samples were repeatedly rinsed with ethanol, subjected to ultrasonic cleaning, and vacuum-dried. Subsequently, the mineral surfaces were treated with different chemical reagents and dried for subsequent use. Surface topography was characterized using a Multimode 8.0 Atomic Force Microscope (Bruker Dimension ICON) operated in Tapping Mode™. In this mode, a microcantilever probe oscillates at high frequency near the sample surface, and surface features are detected through interactions between the probe tip and the sample surface mediated by van der Waals forces. Silicon nitride probes with silicon tips were employed for imaging, utilizing a resonant frequency of 70 kHz. Image acquisition and data analysis were performed using Nanoscope Analysis 1.7 software.

3. Results of flotation

3.1. The influence of feed particle size

Investigation of the impact of feed particle size (-0.5 mm, -0.3 mm, -0.2 mm, -0.15 mm) on the desulfurization efficiency of coal slime flotation was conducted at a pulp density of 45 g/L. Flotation tests were performed under the following reagent conditions: depressant (CaO) dosage of 300 g/t, frother (pine oil) dosage of 300 g/t, oxidant ($Ca(ClO)_2$) dosage of 500 g/t (with an action time of 6 min), and collector (kerosene) dosage of 800 g/t. The results are presented in Fig. 3. When the particle size of the feed coal was -0.2 mm, both the ash content and sulfur content of the clean coal were relatively low, at 11.10% and 1.16%, respectively, with a corresponding clean coal yield of 89.31%. The improved desulfurization efficiency at this size fraction may be attributed to more effective liberation of pyrite achieved through grinding. However, further reducing the coal particle size to -0.15 mm resulted in an increase in both the sulfur and ash content. This deterioration in separation efficiency is likely due to the excessively fine particle size of the coal slime.

3.2. The influence of oxidant consumption

The influence of $Ca(ClO)_2$ dosage, varied from 0 to 1000 g/t, on desulfurization efficiency was investigated under the following conditions: feed particle size of -0.2 mm, kerosene dosage of 800 g/t,

pine oil dosage of 300 g/t, CaO dosage of 300 g/t, and a $Ca(ClO)_2$ action time of 6 minutes. As illustrated in Fig. 4, the clean coal yield and ash content remained relatively stable. However, the clean coal sulfur content exhibited a trend of initial decrease followed by an increase with rising $Ca(ClO)_2$ dosage. Specifically, when no oxidant was added ($Ca(ClO)_2$ dosage = 0 g/t), the clean coal product had a sulfur content of 1.32%, an ash content of 11.89%, and a yield of 89.91%. The lowest sulfur content in the clean coal (1.17%) was achieved at a $Ca(ClO)_2$ dosage of 500 g/t, with corresponding ash content and yield of 11.30% and 89.01%, respectively. This condition demonstrated enhanced desulfurization efficiency.

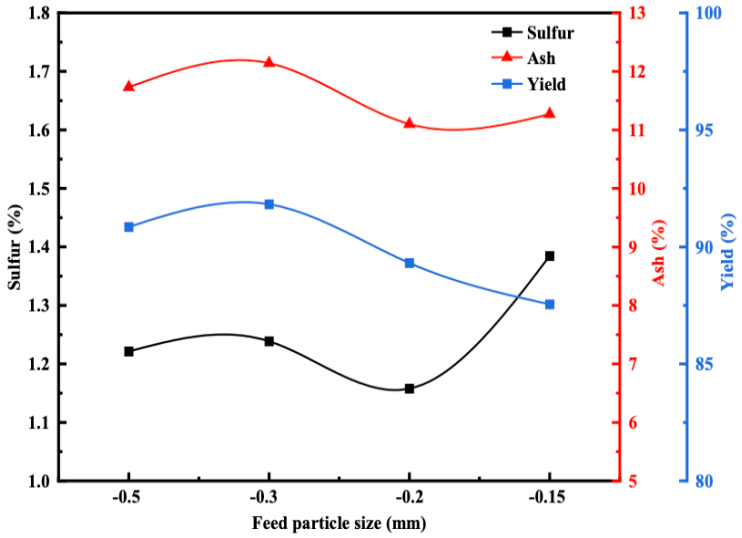

Fig. 3. Effect of raw coal particle size on flotation desulfurization

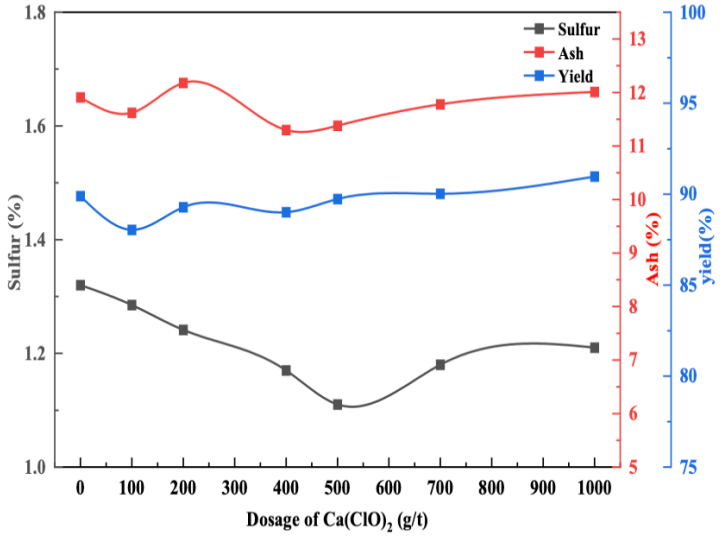

Fig. 4. Effect of $Ca(ClO)_2$ dosage on flotation desulfurization

3.3. The influence of oxidation duration

The preceding experimental results suggest that the intensity of oxidation may influence desulfurization efficiency. Consequently, flotation tests were conducted to investigate the effect of $Ca(ClO)_2$ oxidizing time duration on the desulfurization of coal slime under the following fixed reagent conditions: kerosene dosage of 800 g/t, pine oil dosage of 300 g/t, $Ca(ClO)_2$ dosage of 500 g/t, and CaO dosage of 300 g/t. As shown in Fig. 5, the clean coal yield and ash content exhibited minimal variation with increasing oxidation duration. Notably, however, the clean coal sulfur content displayed a distinct trend of initial decrease followed by a subsequent increase as the $Ca(ClO)_2$ oxidizing duration increased. The lowest sulfur content (1.10%) of the clean coal was achieved at an oxidizing time of 9 minutes, with corresponding ash content and yield of 10.76% and 89.07%, respectively, indicating enhanced

desulfurization efficiency under this condition. Further prolonging the oxidation duration resulted in a deterioration of the flotation desulfurization efficiency.

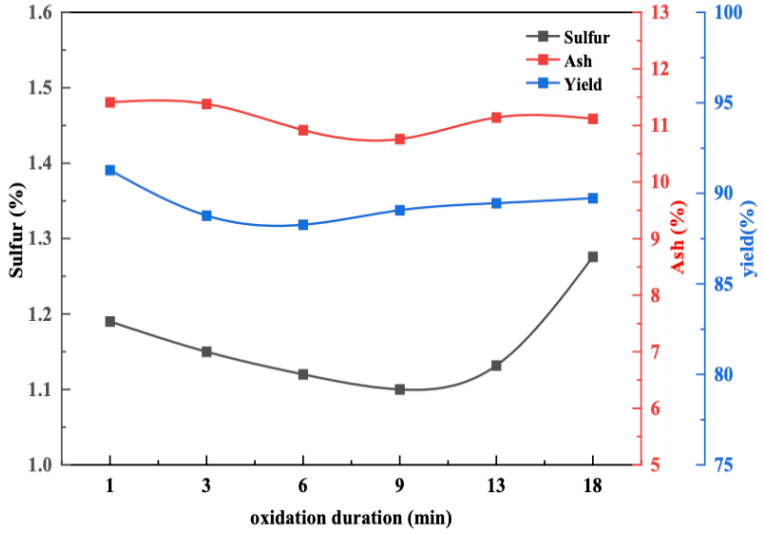

Fig. 5. Effect of $Ca(ClO)_2$ duration on flotation desulfurization

3.4. The influence of depressant consumption

As a commonly used depressant, CaO exerts a significant influence on desulfurization efficiency. To explore the potential for further enhancement of desulfurization, flotation tests were conducted to investigate the effect of CaO dosage on coal slime desulfurization under the following fixed conditions: kerosene dosage of 800 g/t, pine oil dosage of 300 g/t, $Ca(ClO)_2$ dosage of 500 g/t, and an oxidizing duration of 9 minutes. As depicted in Fig. 6, the ash content exhibited minimal variation with increasing CaO dosage. However, the sulfur content of the clean coal demonstrated an initial decrease followed by an increase, while the clean coal yield showed a discernible decreasing trend. The lowest sulfur content (1.10%) of the clean coal was achieved at a CaO dosage of 300 g/t, accompanied by an ash content of 11.21% and a yield as high as 90.64%. This finding suggests that an excessively high dosage of the depressant CaO is detrimental to the process.

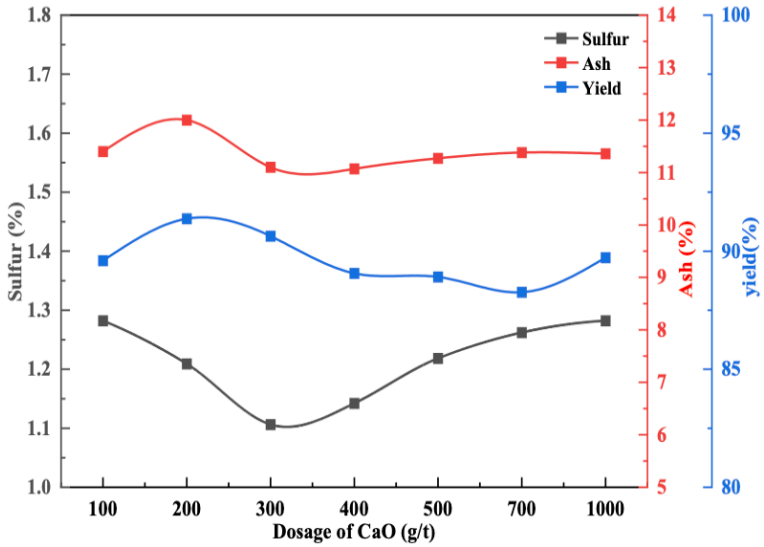

Fig. 6. Effect of CaO dosage on flotation desulfurization

3.5. Flotation flowsheet

Building upon the results of the preceding single-factor conditional tests, a "one roughing-one cleaning" process was explored. As illustrated in Fig. 7, the process commenced with a roughing stage conducted

under the following conditions: oxidant $Ca(ClO)_2$ dosage of 500 g/t, oxidation duration of 9 min, depressant CaO dosage of 300 g/t (action time 2 min), collector kerosene dosage of 800 g/t, and frother pine oil dosage of 300 g/t. Subsequently, the rougher clean coal concentrate underwent a cleaning stage under the conditions: supplementary $Ca(ClO)_2$ dosage of 100 g/t, oxidation time of 3 min, and pine oil dosage of 100 g/t. Detailed experimental results are presented in Table 4.

By implementing the "one roughing-one cleaning" separation process, incorporating pulp oxidation treatment with $Ca(ClO)_2$ during both the roughing and cleaning stages, a final clean coal product was obtained with a sulfur content of 1.04%, an ash content of 11.37%, and a yield of 84.73%. These product parameters essentially met the basic quality requirements for coking coal (sulfur content≤1.0%, ash content≤12.5%).

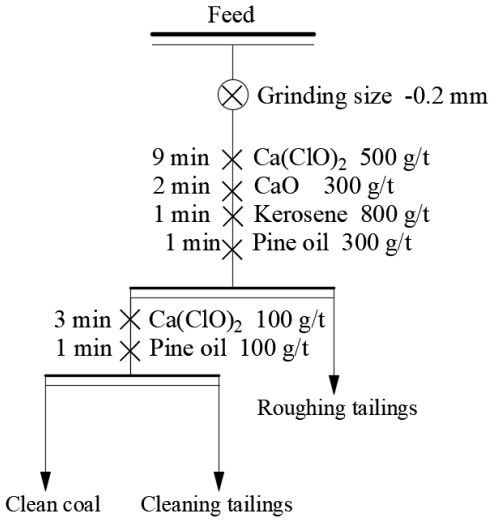

Fig. 7. Coal slime flotation process

Table 4. Coal slime flotation test results

stage	product	sulfur (%)	ash (%)	yield of this stage (%)	yield (%)
roughing	roughing clean coal	1.10	11.21	90.64	/
	roughing tailing	7.08	21.46	9.36	/
	Sum.	1.65	12.17	100	/
cleaning	cleaning clean coal	1.04	11.37	93.48	84.73
	cleaning tailing	2.54	8.92	6.52	5.91
	Sum.	1.14	11.47	100	90.64
The feed		1.66	12.72	100	100

4. The inhibitory mechanism of oxidation on pyrite

4.1. The flotation behavior of pyrite

Using pyrite powder samples as the research object, pure mineral flotation tests were conducted under fixed conditions of 500 g/t kerosene, 100 g/t pine oil. The test results are presented in Fig. 8.

When only CaO was added, the flotation ratio of pyrite initially decreased and then increased with increasing CaO dosage. The minimum ratio (21.36%) was observed at a CaO dosage of 300 g/t. Under the condition of adding only H_2O_2, the pyrite ratio also decreased significantly, reaching a minimum value of 18.11% at an H_2O_2 dosage of 500 g/t. These results indicate that a certain dosage of either CaO or H_2O_2 exerts a depressive effect on pyrite flotation, leading to a reduction in its ratio.

Building upon this foundation, we investigated the flotation behavior of pyrite under the combined action of CaO and H_2O_2/$Ca(ClO)_2$. As shown by the red curve in Fig. 8, the minimum flotation recovery of pyrite reached 8.70% and 8.86% when using 300 g/t CaO and 500 g/t H_2O_2/$Ca(ClO)_2$. This value is significantly lower than the ratios observed with either CaO or H_2O_2 alone, indicating that the simultaneous addition of H_2O_2 and CaO produces a synergistic effect, enhancing the depressive effect

on pyrite. Furthermore, both the H_2O_2 dosage and its duration time exhibited a common pattern regarding their impact on pyrite ratio: Within a certain range, increasing the oxidant dosage or extending the action time strengthened the depression of pyrite. However, excessive oxidant dosage or prolonged action time counterintuitively diminished the depressive effect. This demonstrates that the oxidative regulation of the pulp should be controlled to achieve an appropriate oxidation intensity to ensure optimal desulfurization performance.

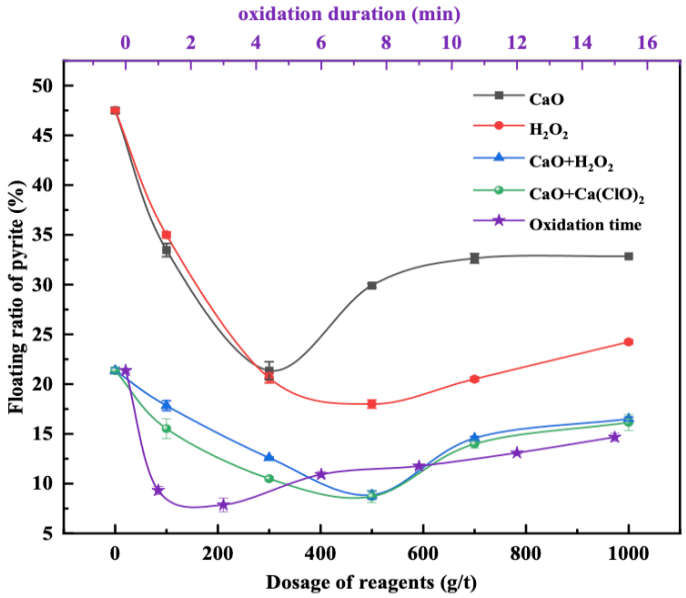

Fig. 8. Effect of reagent dosage and oxidation duration on the floating ratio of pyrite

In Fig. 8, $Ca(ClO)_2$ and H_2O_2 exhibited similar inhibitory performance during oxidant type screening. However, $Ca(ClO)_2$ typically exists in a suspended form, whereas H_2O_2 present as a homogeneous aqueous solution. Since the mechanism section focuses on investigating the effect of oxidation on the surface properties of pyrite, H_2O_2 was selected as a better oxidant. This selection was made to eliminate the effect of suspended $Ca(ClO)_2$ particles on the physical coverage of pyrite surface and confound the experimental results.

4.2. The contact angles

The contact angle measurement results for the pyrite surface are presented in Fig. 9. In the absence of any reagents, the pyrite exhibited a relatively large contact angle of 72.3° (Fig.9-a), indicating its inherent strong hydrophobicity. After treatment with 300 g/t H_2O_2 alone for 3 minutes, the contact angle decreased to 54.1° (Fig. 9-b). Similarly, treatment with 300 g/t CaO alone resulted in a contact angle of 55.7° (Fig. 9-c). These observations demonstrate that the addition of either CaO or H_2O_2 alone enhances the hydrophilicity of the pyrite surface to some extent. Maintaining a constant CaO dosage of 300 g/t, the contact angle showed a trend of initial decrease followed by an increase as the H_2O_2 dosage was raised (with the oxidation duration fixed at 3 minutes). The minimum contact angle observed was 31.3° at an oxidant (H_2O_2) concentration of 500 g/t (Fig. 9-d). The pattern of contact angle changes described above indicates that moderate oxidation in the presence of CaO reduces the surface hydrophobicity of pyrite, thereby enhancing its surface hydrophilicity and leading to a decrease in flotation ratio.

4.3. The coating angles

As shown in Fig. 10, the coating angle formed by particles on bubbles decreased initially and then increased with increasing H_2O_2 dosage. In the absence of reagents, the coating angle was 103.70°, indicating considerable pyrite particle adsorption to the bubble surface (Fig. 10-a). After treatment with 300 g/t H_2O_2 alone for 3 minutes, the coating angle decreased to 89.80° (Fig. 10-b). Similarly, treatment with 300 g/t CaO alone yielded a coating angle of 91.22° (Fig. 10-c). Both values are significantly lower than the angle observed without reagents, demonstrating a depressive effect on pyrite by either CaO or H_2O_2.

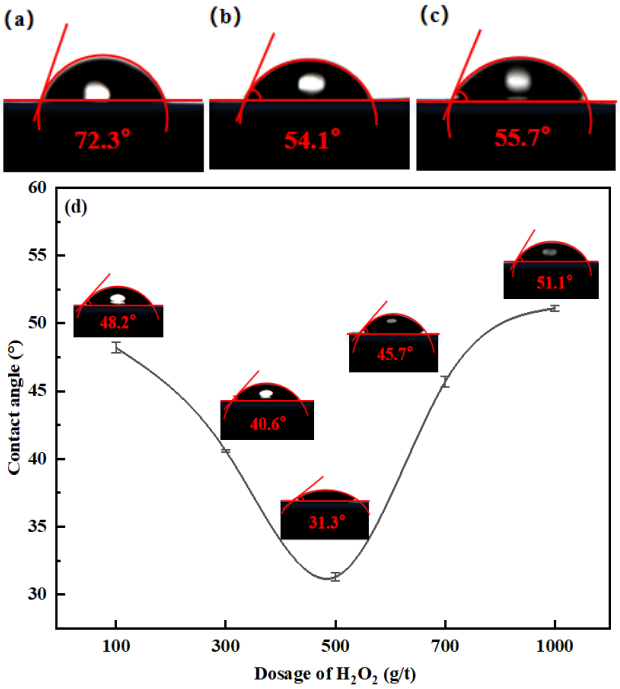

Fig. 9. Effect of different reagent conditions on the contact angle of pyrite, (a) no regent, (b) H_2O_2, (c) CaO, (d) CaO+H_2O_2(variable)

Maintaining a constant CaO dosage of 300 g/t, the coating angle exhibited an initial decrease followed by an increase as the H_2O_2 dosage was raised (with the duration time of 3 minutes). A minimum coating angle of 57.85° was achieved at an H_2O_2 dosage of 500 g/t (Fig. 10-d), indicating that the synergistic action of CaO and H_2O_2 effectively reduces particle adhesion. The pattern of coating angle changes described above demonstrates that moderate pulp oxidation in the presence of CaO reduces the adsorption of pyrite particles onto bubbles. This reduction in adsorption is directly responsible for the observed decrease in pyrite flotation ratios.

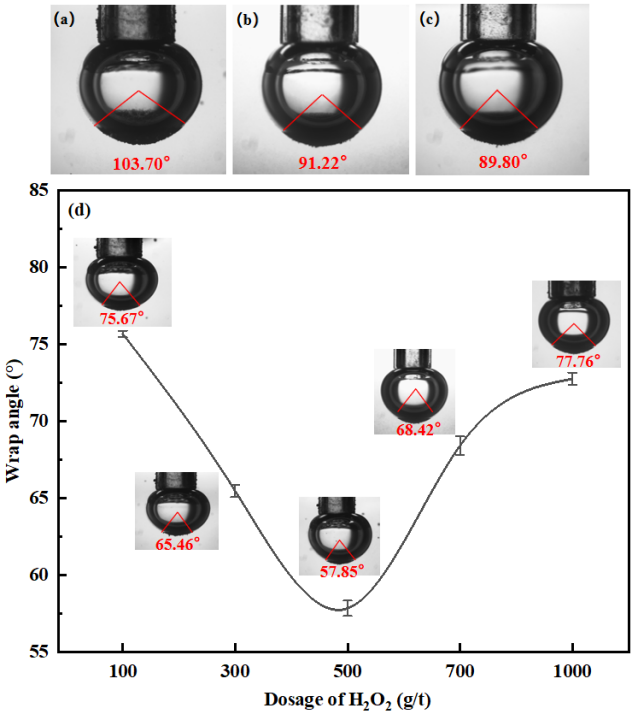

Fig. 10. Effect of different reagent conditions on the coating angle of pyrite, (a) no regent, (b) H_2O_2, (c) CaO, (d) CaO+H_2O_2(variable)

4.4. The induction time

As shown in Fig. 11, the induction time measurements revealed that the shortest induction time required for attachment between pyrite particles and bubbles was 8 ms in the absence of any reagents. When treated with 500 g/t H_2O_2 for 3 minutes, the induction time increased to 15 ms, while treatment with 300 g/t CaO resulted in an induction time of 18 ms. These results demonstrate that the addition of either H_2O_2 or CaO prolongs the time necessary for contact and attachment between pyrite particles and bubbles. Building upon these findings, the effect of the combined action of CaO and H_2O_2 on induction time was investigated. Maintaining a constant CaO dosage of 300 g/t, the induction time between bubbles and particles increased initially and then decreased as the H_2O_2 dosage was increased (with a fixed duration of 3 minutes). The induction time peaked at 50 ms when the H_2O_2 dosage was 500 g/t. This indicates that the combined action of CaO and H_2O_2 significantly prolongs the induction time, thus hindering bubble mineralization (particle loading).

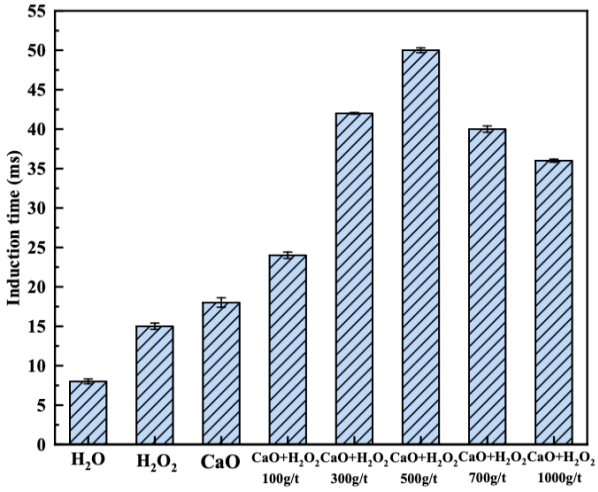

Fig. 11. Effect of different reagent conditions on the induction time

4.5. The wetting heat

The micro-reaction heat between pyrite and water (also known as the wetting heat), reflects the reaction process between pyrite and water. Specifically, if the measured microcalorimetric value is negative, it indicates that the adsorption reaction of water molecules on the pyrite surface is an exothermic process, and this adsorption occurs spontaneously.

As shown in Fig. 12, without any reagents, the wetting heat for pyrite and water was -1.85 J/g. In comparison, when H_2O_2 (500 g/t) and CaO (300 g/t) were added individually, the wetting heat were -1.98 J/g and -1.95 J/g, respectively. Both values are greater (more negative) than that observed without reagents. Simultaneously adding CaO and H_2O_2 to the pulp further increased the heat of wetting. Specifically, at a fixed CaO dosage of 300 g/t, the wetting heat between pyrite and water initially increased and then decreased as the H_2O_2 dosage increased (with a reaction duration of 3 minutes). The wetting heat reached a maximum value of -3.66 J/g at an H_2O_2 dosage of 500 g/t. This essentially explains that after treatment with both H_2O_2 and CaO, the reaction intensity between the pyrite surface and water molecules is significantly greater. This manifests as enhanced hydrophilicity and reduced hydrophobicity of the pyrite surface, resulting in the depression of pyrite flotation.

4.5. Surface material characteristics

4.5.1. Surface microscopic morphology

Given that oxidation occurs exclusively on the mineral surface, it is necessary to investigate the effect of oxidation on the surface morphology of pyrite. Evidence suggests that oxidation may preferentially initiate at surface defects, leading to an increase in the hydrophilicity of the mineral surface (Tu et al. 2017., Ramírez-Aldaba et al., 2016). AFM was employed to analyze the distribution of dendritic protrusions on the pyrite surface following oxidation treatment with different reagents. The three-

dimensional topographies of the pyrite surface before and after oxidation are presented in Fig. 13.

As observed in Fig. 13-a, the unoxidized pyrite surface exhibited a certain degree of roughness, with a root mean square (RMS) roughness of 22.6 nm, attributable to scratches introduced during the polishing process. When CaO or H_2O_2 was added individually, a small number of dendritic protrusions appeared on the pyrite surface (Fig. 13-b and 13-c). The corresponding RMS roughness values were 35.2 nm and 38.3 nm, respectively, representing a significant increase compared to the pre-oxidation state. This increase is likely due to surface corrosion induced by oxidation and the accumulation of oxidation products on the mineral surface. Under the simultaneous addition of CaO and H_2O_2, a substantial quantity of dendritic protrusions was observed on the pyrite surface (Fig. 13-d), and the RMS roughness reached 85.5 nm. This value is markedly higher than those obtained with either reagent alone. These results indicate that the combined action of H_2O_2 and CaO significantly increased the surface roughness of pyrite. Integrating this finding with data from pure mineral flotation tests and discussion above, it is postulated that the increased surface roughness may be one factor hindering the attachment between the mineral particles and air bubbles, thereby inhibiting flotation.

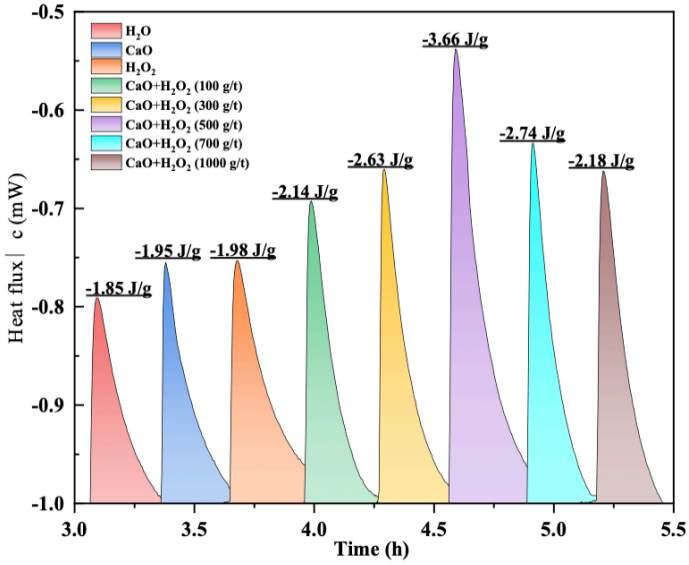

Fig. 12. Effect of different reagent conditions on the wetting heat

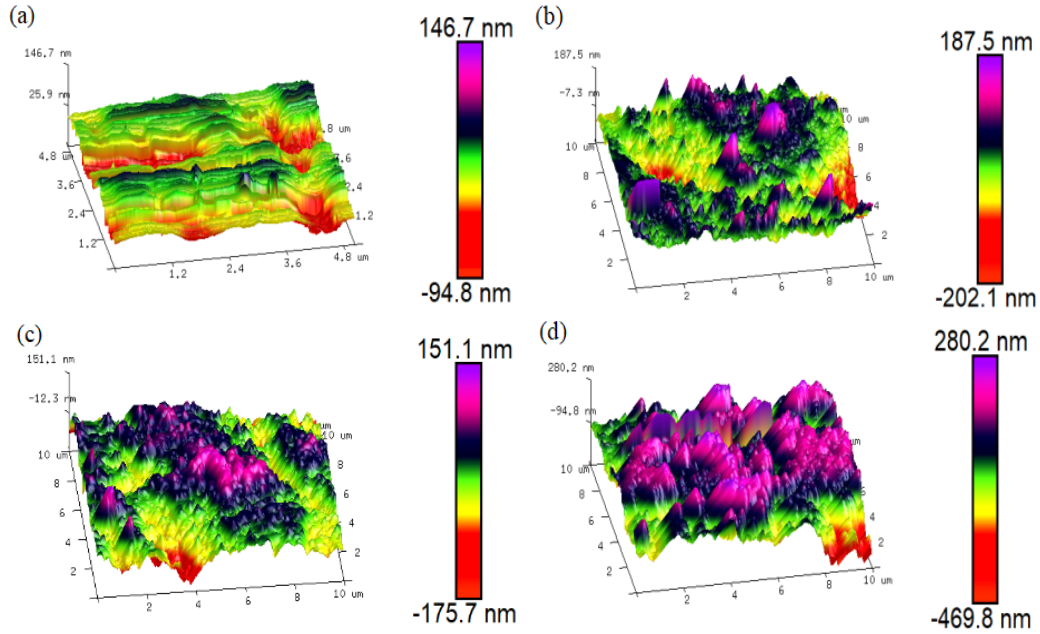

Fig. 13. AFM images of pyrite samples treated with different reagents (a) no treatment, (b) CaO, (c)H_2O_2, (d) CaO+H_2O_2

4.5.2. Surface material composition

Microscopic confocal raman spectroscopy was employed to analyze the surface composition of pyrite samples treated with CaO, H_2O_2, and CaO+H_2O_2, as presented in Fig. 14. As shown in Fig. 14-a, the surface of the untreated sample exhibited characteristic spectral features corresponding to pyrite (blue regions) and coal organic matter (red regions). Characteristic vibrational bands of pyrite were detected within the wavenumber ranges of 342.3-344.4 cm^{-1}, 378.7-380.4 cm^{-1}, and 431.6-432.2 cm^{-1}. These bands are assigned to Fe-S bond deformation vibration, Fe-S bond stretching vibration, and S-S bond stretching vibration modes, respectively (Gao et al., 2022; Zhang et al., 2025).

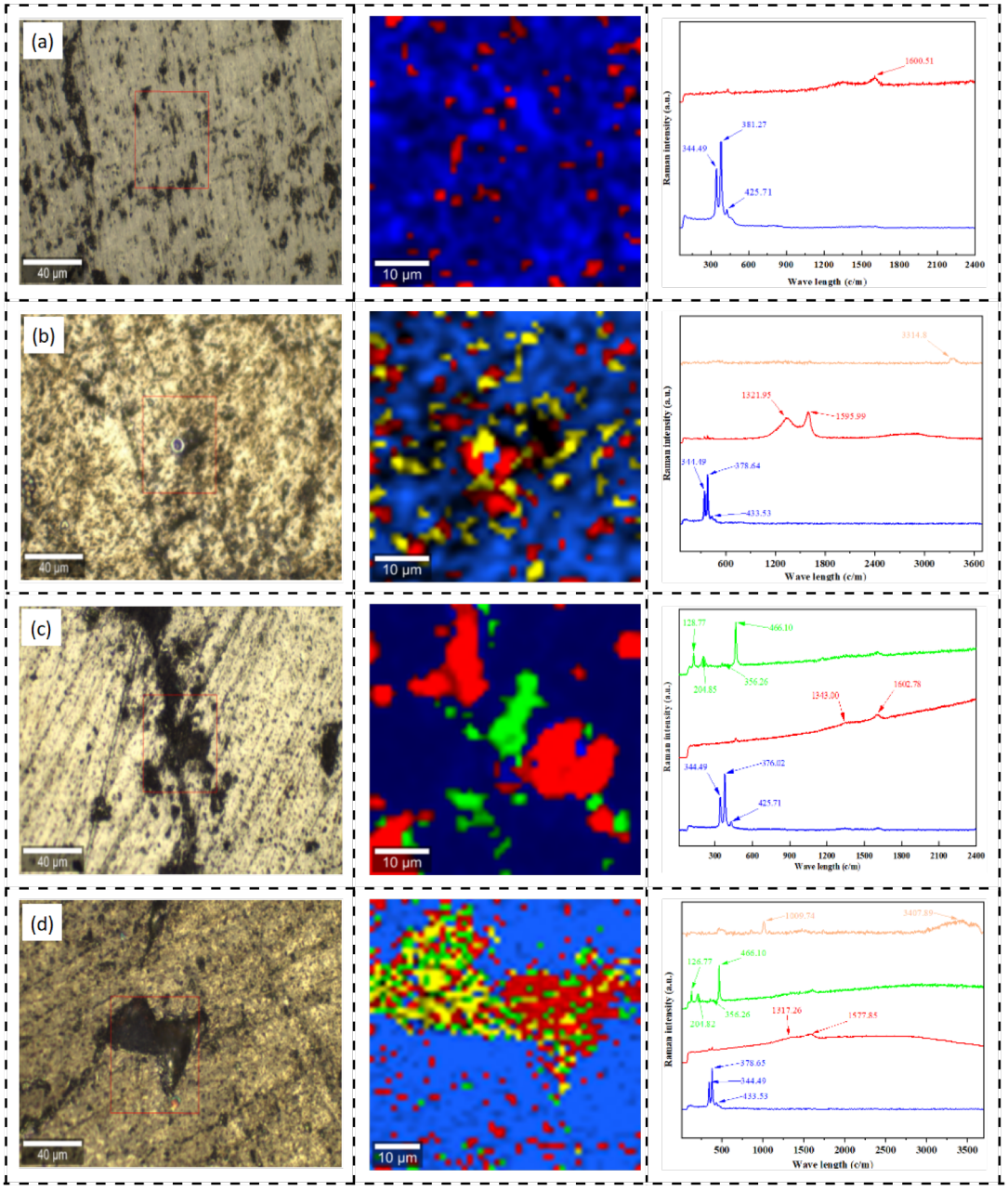

Fig.14. Microscopic imaging, Raman imaging and spectra of pyrite under different reagents (a) no treatment, (b) CaO, (c) H_2O_2, (d) CaO+H_2O_2

Following treatment with CaO, the pyrite characteristic band intensities exhibited an observable decrease (Fig. 14-b). The Ca-OH band is the most intense and sharpest peak within the O-H symmetric stretching region (3100-3700 cm^{-1}). Therefore, the band observed at 3314.8 cm^{-1} is attributed to $Ca(OH)_2$, indicating that the addition of CaO likely resulted in the adsorption and deposition of a small amount

of calcium-containing species on the pyrite surface. This process did not involve a strong chemical reaction with the pyrite surface generating new reaction products (Tian et al., 2020). As shown in Fig. 14-c, the peak intensities of pyrite decreased after H_2O_2 treatment, signifying a significant alteration in its surface composition. The Raman spectrum of pyrite displayed a substantial increase in the number of additional peaks alongside peak broadening (increased full width at half maximum). Specifically, characteristic bands of Fe_2O_3 appeared near 204.85 cm^{-1} and 356.26 cm^{-1} (Kirik et al., 2023), and bands characteristic of $Fe(OH)_3$ were detected near 128.77 cm^{-1} and 466.10 cm^{-1} (Yoon et al., 2024). This demonstrates that oxidation occurred on the pyrite surface, leading to the accumulation of oxidation products. Fig. 14-d reveals that under the combined action of CaO and H_2O_2, the pyrite band intensities were further reduced. Concurrently, the intensities of the characteristic bands for Fe_2O_3, $Fe(OH)_3$, and $Ca(OH)_2$ increased. Furthermore, a Raman band corresponding to SO_4^{2-} appeared at 1009.74 cm^{-1} (within the characteristic range of 980-1020 cm^{-1}) (Schmidt et al., 2017). These observations indicate an intensified oxidation of the pyrite surface under these conditions, generating species such as $Ca(OH)_2$, iron oxides, and sulfates (e.g., $Fe_2(SO_4)_3$, $CaSO_4$). These compounds are the primary contributors to the enhanced hydrophilicity of the pyrite surface. Synthesizing the preceding analyses, it is evident that slurry oxidation treatment induces oxidation on the pyrite surface. Particularly under the combined action of CaO and H_2O_2 at moderate oxidation intensity, the pyrite surface accumulates hydrophilic species such as $Fe_2(SO_4)_3$, $CaSO_4$, and $Ca(OH)_2$. This accumulation leads to: (a) increased surface roughness, (b) decreased contact angle and wetting angle, (c) prolonged induction time, and (d) Enhanced wetting heat. These observations collectively demonstrate that the controllable oxidation treatment of the pulp effectively enhances the hydrophilicity of pyrite, consequently diminishing its floatability (Fig. 15). This explains the underlying mechanism by which slurry oxidation facilitates the deep desulfurization of coal fines.

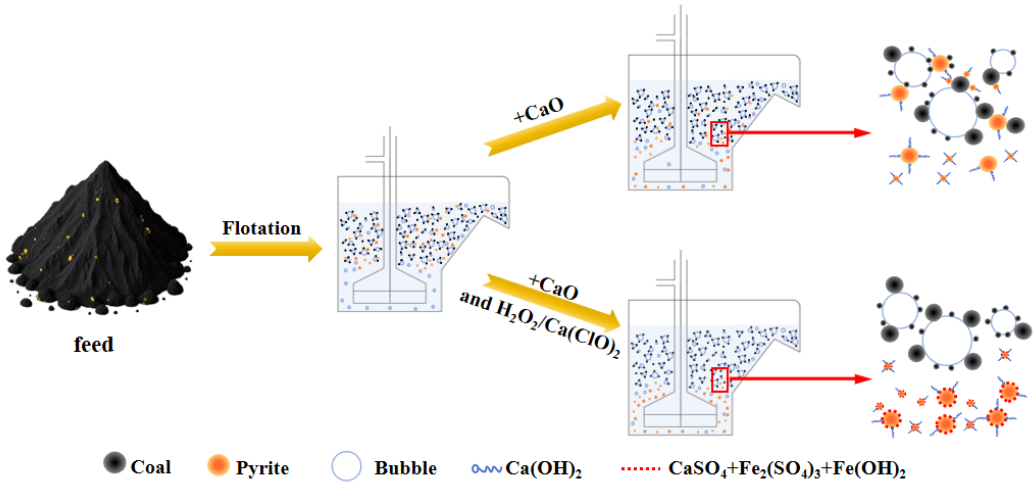

Fig. 15. Schematic diagram of moderate oxidation of flotation pulp for deep desulfurization of fine coking coal

5. Conclusions

Flotation was employed for the desulfurization of coking coal with an initial sulfur of 1.66%. Under the conditions of a grind size of -0.2 mm, CaO 300 g/t, kerosene 800 g/t, and pine oil 300 g/t, a single roughing flotation stage yielded a clean coal product with a sulfur of 1.32% and an ash of 11.89%. The clean coal yield was 89.91%. Building upon this, the slurry oxidation method was implemented in a "one roughing-one cleaning" flowsheet. In the roughing stage, the $Ca(ClO)_2$ was added at 500 g/t and conditioned for 9 minutes. Subsequently, in the cleaning stage, $Ca(ClO)_2$ was added at 100 g/t and conditioned for 3 minutes. Following this, a final clean coal product was achieved with a sulfur of 1.04% and an ash of 11.37%. The clean coal yield reached 84.73%.

Through pure mineral flotation tests and measurements of contact angle, coating angle, induction time, and wetting heat, it was found that after adding an oxidant to the slurry with moderate oxidation intensity, the contact angle on the pyrite surface decreased, the coating angle of particles on bubbles reduced, the particle-bubble induction time prolonged, and the wetting heat between pyrite and water

molecules increased. These changes ultimately led to a decrease in the floatability of pyrite. Analyses of AFM and Raman spectroscopy confirmed that the oxidant can accelerate the surface oxidation process, promoting the formation of hydrophilic products such as $Fe_2(SO_4)_3$, $CaSO_4$, and $Ca(OH)_2$. The coating formed by these products on the pyrite surface weakens the surface hydrophobicity, resulting in the inhibition of pyrite during flotation.

Acknowledgement

This study was supported by Key Support Project of Regional Innovation and Development Joint Fund of National Natural Science Foundation of China (U24A2095).

References

BAI, S., YU, P., LI, C., WEN, S., DING, Z., 2019. *Depression of pyrite in a low-alkaline medium with added calcium hypochlorite: Experiment, visual MINTEQ models, XPS, and ToF-SIMS studie.* Miner. Eng. 141, 105853.

BULUT, G., CEYLAN, A., SOYLU, B., GOKTEPE, F., 2012. *Role of starch and metabisuphite on pure pyrite and pyritic copper ore flotation*. Physicochem. Probl. Miner. Process. 48, 261902-92104.

CAO, Q., YAN, W., LIU, D., WEN, S., AND LI, Y., 2023. *New insights into pyrite-hydrogen peroxide interactions during froth flotation: experimental and DFT study.* Physicochem. Probl. Miner. Process. 59, 157409.

CHENG, G., LI, Y., CAO, Y., WANG, X., LI, E., GUO, Y., LAU, E., 2024. *New Insights on the Understanding of Sulfur-Containing Coal Flotation Desulfurization*. Minerals. 14, 981.

CHEN, M., BI, Y., DING, Z., YUAN, J., YU, A., CHEN, L., BAI, S., MAO, Y., 2024. *Application of calcium hypochlorite and carboxymethyl chitosan as combined depressants for selective flotation separation of chalcopyrite from pyrite at low alkalinity*. Adv. Powder. Technol. 35, 104649.

CHOU, C., 2012. *Sulfur in coals: A review of geochemistry and origins.* Int. J. Coal. Geol. 100, 1-13.

DAI, S., FINKELMAN, R., FRENCH, D., HOWER J., GRAHAM, I., ZHAO, F., 2021. *Modes of occurrence of elements in coal: A critical evaluation.* Earth-Sci. Rev. 222, 103815.

DEBIAGI, P., YILDIZ, C., RICHTER, M., STRÖHLE, J., EPPLE, B., FARAVELLI, T., HASSE, C., 2021. *Experimental and modeling assessment of sulfur release from coal under low and high heating rates.* P. Combust. Inst. 38, 4053-4061.

DIEHL, S., GOLDHABER, M., KOENIG, A., LOWERS, H.A., RUPPERT. L., 2012. *Distribution of arsenic, selenium, and other trace elements in high pyrite Appalachian coals: Evidence for multiple episodes of pyrite formation.* Int. J. Coal Geol. 94, 238-249.

ERCAN, S., 2018. Cleaning of high pyritic sulfur fine coal via flotation, Adv. Powder Technol. 29(7) (2018) 1703-1712.

FLETCHER, B., CHIMONYO, W., PENG, Y., 2020. *A comparison of native starch, oxidized starch and CMC as copper-activated pyrite depressants*. Miner. Eng. 156, 106532.

GAN, G., LI, Y., CAO, Y., ZHANG, Z., 2023. A novel method for the desulfurization of medium-high sulfur coking coal, Fuel 335 (2023) 126988.

GAO, S., HUANG, F., LIU, J., SU, L., WANG, W., 2025. *In Situ Raman Spectra Characterization of Zonal Arsenic-Bearing Pyrite and Arsenopyrite in the Baiyunpu Gold Deposit.* Hunan. Spectrosc. Spect. Anal. 40, 2525.

GUO, B., PENG, Y., ESPINOSA-GOMEZ, R., 2014. *Cyanide chemistry and its effect on mineral flotation.* Miner. Eng. 66-68, 25-32.

HAN, G., WEN, S.M., WANG, H., FENG, Q., 2019. *Lactic acid as selective depressant for flotation separation of chalcopyrite from pyrite and its depression mechanism.* J. Mol. Liq. 296, 111774.

HE, J., LIU, C., YAO, Y., 2018. *Flotation intensification of the coal slime using a new compound collector and the interaction mechanism between the reagent and coal surface*. Powder Technol. 325, 333-339.

HOU, H., CHENG, W., LI, X., 2025. *Effect of dodecane on the floatability of coal-bearing pyrite and common pyrite: An experimental and molecular simulation study.* Appl. Surf. Sci. 688, 162392.

HOU, H., CHENG, W., YANG, R., ZHANG, Y., 2024. *The abundance, distribution, and enrichment mechanism of harmful trace elements in coals from Guizhou, Southwestern China*. Acta Geochim. 43, 889-903.

HOU, H., PAN, X., CHENG, W., HUANG, X., LI, X., 2025. *Oxidative slurry pretreatment for enhanced desulfurization of high-sulfur coal*. Colloids Surf., A. 725, 13768.

HUANG, X., ZHANG, Q., 2025. *Surface characteristics and dispersion behaviours of fluorapatite and dolomite in the presence of $H_2PO_4^-$ in grinding environment.* Miner. Eng. 232, 109473.

JIANG, K., LIU, J., WANG, Y., ZHANG,D., HAN, Y., 2022. *Surface properties and flotation inhibition mechanism of air oxidation on pyrite and arsenopyrite.* Appl. Surf. Sci. 610, 155476.

JIAO, L., YANG, R., CHEN, B., ZHANG, Y., 2023. *Variation, Determinants and prediction of carbon emissions in Guizhou, a new economic growth pole in southwest China*. J. Cleaner Prod. 417, 138049.

KAAWATRA, S., EISELE, T., 1992. *Removal of Pyrite in Coal Flotation*. Miner. Process. Extr. Metall. Rev. 8, 205-218.

KIRIK, N., KRYLOV, A., BORONIN, A., KOSHCHEEV, S., SOLOVYOV, L., RABCHEVSKII, E., SHISHKINA, N., ANSHITS, A., 2023. *The Relationship between the Structural Characteristics of a-Fe_2O_3 Catalysts and Their Lattice Oxygen Reactivity Regarding Hydrogen.* Materials. 16, 4466.

LI, C.W., ZHEN, K., HAO, Y., ZHANG, H., 2018. *Effect of dissolved gases in natural water on the flotation behavior of coal*. Fuel. 233, 604-609.

LI, Y., CHENG, G., ZHANG, M., CAO, Y., LAU, V., 2022. *Advances in depressants used for pyrite flotation separation from coal/minerals*. Int. J. Coal Sci. Technol. 9, 54.

MU, X., JIN, Z., DENG, C., GAO, F., 2020. Variation of Sulfur Content in Coking Coal as Function of Its Particle Size. Solid. Fuel. Chem. 54, 326–336.

MUNAWER, M., 2018. *Human health and environmental impacts of coal combustion and post-combustion wastes*. J. Sustain. Min. 17, 87-96.

MAZHAR, M., KHAN, N., AHMED, S., KHAN, A., HUSSAIN, A., RAHISUDDIN., CHANGANI, F., YOUSEFI, M., AHMADI, S., VAMBOL, V., 2020. *Chlorination disinfection by-products in municipal drinking water – A review*. J. Cleaner Prod. 273, 123159.

PHENGSAART, T., SRICHONPHAISAN, P., KERTBUNDIT, C., SOONTHORNWIPHAT, N., SINTHUGOOT, S., PHUMKOKRUX, N., JUNTARASAKUL, O., MANEEINTR, K., NUMPRASANTHAI, A., PARK, I., TABELIN, C., HIROYOSHI, N., ITO, M., 2023. *Conventional and recent advances in gravity separation technologies for coal cleaning: A systematic and critical review.* Heliyon. 9, e13083.

PRAKASH, J., AGRAWAL, S., AGRAWAL, M., 2023. *Global Trends of Acidity in Rainfall and Its Impact on Plants and Soil*. J. Soil. Sci. Plant. Nutr. 23, 398-419.

PI, L., CAI, J., XIONG, L., CUI, J., HUA, H., TANG, D., MAO, X., 2020. *Generation of H_2O_2 by on-site activation of molecular dioxygen for environmental remediation applications: A review*. Chem. Eng. J. 389, 123420.

QI, X., LI, X., LIANG, Y., WANG, H.N., GUO, W., CONG, X., LV, F., ZHANG, H., 2020. *Surface structure-dependent hydrophobicity/oleophilicity of pyrite and its influence on coal flotation.* J. Ind. Eng. Chem. 87, 136-144.

QI, X., ZHANG, H., LI, Y., CHEN, J., 2019. *Density functional theory study of the structure and properties of C-doped pyrite*. 572, 168-174.

R.P. Liao, S.M. Wen, Q.C. Feng, J.S. Deng H. Lai, Activation mechanism of ammonium oxalate with pyrite in the lime system and its response to flotation separation of pyrite from arsenopyrite, Int. J. Miner. Metall. Mater. 30 (2023) 271.

RAMÍREZ-ALDABA, H., VALLES, O., VAZQUEZ-ARENAS, J., ROJAS-CONTRERAS, J., VALDEZ-P´EREZ, D., RUIZ-BACA, E., MERAZ-RODRÍGUEZ, M., SOSA-RODRÍGUEZ, F., RODRÍGUEZ, A., LARA, R., 2016. *Chemical and surface analysis during evolution of arsenopyrite oxidation by Acidithiobacillus thiooxidans in the presence and absence of supplementary arsenic.* Sci. Total Environ. 566-567, 1106-1119.

SCHMIDT, C., SEWARD, T., 2017. *Raman spectroscopic quantification of sulfur species in aqueous fluids: Ratios of relative molar scattering factors of Raman bands of H_2S, HS^-, SO_2, HSO_4^-, SO_4^{2-}, $S_2O_3^{2-}$, S_3^- and H_2O at ambient conditions and information on changes with pressure and temperature.* Chem. Geol. 467, 64-75.

TANG, L., CHEN, S., GUI, D., ZHU, X., HE, H., TAO, X., 2020. *Effect of removal organic sulfur from coal macromolecular on the properties of high organic sulfur coal*. Fuel. 259, 116264.

TIAN, Z., ZHANG, X., LIU, C.L., MENG, Q., DU, Z., YAN, J., 2020. *Characterization of the Influence of Hydrated Ions on the Oxygen-Hydrogen Stretching Vibration of Water by Raman Spectroscopy.* Anal. Lett. 53, 2034-2046.

TU, Z., WAN, J., GUO, C., FAN, C., ZHANG, T., LU, G., REINFELDER, J., DANG, Z., 2017. *Electrochemical oxidation of pyrite in pH 2 electrolyte.* Electrochim. Acta. 239, 25-35.

WANG, C., CEN, X., XING, Y.W., ZHANG, C., LI, J., GUI, X., 2023. *Depression mechanisms of sodium humate and 3-mercaptopropionic acid on pyrite in fine coal flotation.* Appl. Surf. Sci. 613, 156151.

XIA, W., XIE, G., 2017. *A technological review of developments in chemical-related desulfurization of coal in the past decade.* Int. J. Miner. Process. 161, 65-71.

YANG, X., LI, Y., FAN, R., DUAN, W., HUANG, L., XIAO, Q., 2022. *Separation mechanism of chalcopyrite and pyrite due to H_2O_2 treatment in low-alkaline seawater flotation system.* Miner. Eng. 176, 107356.

Yoon, G., Jang, Y., Jang, H.S., Lee, S., Ryu, G., 2024. *Facile synthesis and electrochemical properties of $FeO/Fe(OH)_3$ nanosheets.* Appl. Surf. Sci. 682, 161621.

ZHANG, G., DU, Y., ZHANG, Y., XU, Y., 2014. *Desulfurization reaction model and experimental analysis of high sulfur coal under hydrogen atmosphere*. J. Ind. Eng. Chem. 20, 487-493.

ZHANG, H., DOU, B., ZHANG, H., LI, J., RUAN, C., WU, C., 2020. *Study on non-isothermal kinetics and the influence of calcium oxide on hydrogen production during bituminous coal*. J. Anal. Appl. Pyrol. 150, 104888.

ZHANG, H., QIAN, G., CAI, Y., GIBSON C., PRING, A., 2022. *Crystal chemistry of arsenian pyrites: A Raman spectroscopic study.* Am. Mineral. 107, 274-281.

ZHAO, H., BAI, Z., GUO, Z., KONG, L., YUCHI, W., LI, H., BAI, J., LI, W., 2021. *In situ study of the decomposition of pyrite in coal during hydropyrolysis.* J. Anal. Appl. Pyrolysis. 154, 105024.

ZHAO, H., NIU, X., DONG, B., JIA, X., RUAN, R., 2022. *Investigation on the correlation between ferrous ion and the floatability of pyrite with different oxidation degrees.* Miner. Eng. 184, 107636.

ZHOU, Y., ALBIJANIC, B., TADESSE, B., WANG, Y., YANG, J., ZHU, X., 2019. *Flotation behavior of pyrite in sub-bituminous and meta-bituminous coals with starch depressant in a microflotation cell*. Fuel Process. Technol. 187, 1-15.